Saturation Control of a Piezoelectric Actuator for Fast Settling-Time Performance

Jinchuan Zheng and Minyue Fu, *Fellow, IEEE*

Abstract—**This brief studies fast tracking control of piezoelectric (PZT) actuators. Adverse effects associated with the PZT actuators typically include the nonlinear dynamics of hysteresis and saturation and the linear vibrational dynamics. To eliminate the loss of performance due to these effects, we propose a new control scheme for the PZT actuators. It consists of a combined feedforward/feedback compensator for hysteresis and resonance compensation and a nested switching controller (NSC) that optimizes a quadratic performance cost function involving the actuator saturation. The NSC not only can guarantee the system stability in the presence of saturation but also can improve the tracking speed by efficiently allocating the control efforts. The experimental results on an actual PZT nanopositioner show that the new control scheme outperforms the conventional control by more than 12% in settling time within the full PZT operational range and with nanoscale precision.**

Index Terms—**Actuator saturation, hysteresis, motion control, piezoelectric (PZT) actuator, switching control.**

I. INTRODUCTION

THE PIEZOELECTRIC (PZT) actuator is a well-known device for precision positioning control, which can produce small displacements in the range of subnanometer to a few hundreds micrometers. PZT actuators have been widely used in a variety of applications such as optical trapping [1], nanomanipulation [2], atomic force microscope (AFM) [3].

Nonlinear hysteresis and creep effects are common properties with PZT actuators, which degrade the positioning precision. It has been reported that hysteresis effects can be reduced by the use of charge or current sources to drive the PZT actuators (see, e.g., [4], [5]). However, the main difficulty is the existence of offset voltages in the charge or current source circuit and the uncontrolled nature of the output voltage, which results in capacitive load being charged up [6]. Additionally, commercial charge amplifiers are not commonly available. Alternatively, the use of voltage amplifier combined with servo control is a popular approach for its easy implementation and its capability to effectively eliminate the hysteresis and creep effects.

A thorough literature review on control approaches for PZT actuators is reported in [6] and [7]. In particular, for hysteresis

J. Zheng is with the School of Robotics and Mechatronics, Swinburne University of Technology, Hawthorn, VIC 3122, Australia (e-mail: jimjeng806@hotmail.com).

M. Fu is with the School of Control Science and Engineering, Zhejiang University, Hangzhou 310058, China (e-mail: minyue.fu@newcastle.edu.au).

and vibration compensations there are two main approaches: inversion-based feedforward [8] and high-gain feedback [9]. In the inversion-based feedforward approach, an accurate hysteresis and vibrational dynamic model is crucial because the desired output is fed through the inverse model to generate feedforward signals to cancel the hysteresis and vibrations. For this reason, a variety of hysteresis models are reported (see, e.g., [10], [11]) to capture the hysteresis behavior. However, such feedforward-based methods are essentially open-loop control systems and thus the performance is sensitive to modeling errors. In contrast, the high-gain feedback approach avoids the need for an accurate model. In such methods [9], hysteresis and vibrations are essentially regarded as input disturbances and the induced position error is then corrected by the PZT feedback controller. In addition, Leang has also proposed a combined feedforward-feedback control approach, where the high-gain feedback control is used to linearize the nonlinear hysteresis and creep, and a feedforward input is found to deal with vibrations [12].

Tracking control is another main control task for the PZT actuators, which aims to drive the position output to track a desired trajectory such as triangular waveforms in AFM applications [13], and step references in pick-and-place operations [9]. To achieve this task, traditional proportional-integral-derivative (PID) controllers are generally used [9]. Furthermore, advanced control methods are also reported which, for example, include robust control [14], adaptive control [15], iterative control [16], and preview-based optimal inversion method [17]. However, in most existing literature, the PZT actuator saturation nonlinearity is rarely explicitly considered in the control design. Typically, due to the PZT actuator limited travel range, the control input should be constrained to avoid damage to the PZT ceramics. Nevertheless, most existing controllers are designed either by ignoring the saturation nonlinearity or by constraining the control input not to hit the saturation limit. Each of the above methods has its own disadvantages, especially for step tracking control. The first disadvantage is that when the PZT actuator works around its maximum range, the performance may deteriorate (e.g., causing excessive oscillations) once a large disturbance occurs because the control design does not guarantee fast convergence of the closed-loop system in the presence of saturation. The second one is that when the PZT actuator works in a small range, the allowable control input is not fully used, thus resulting in conservative performance (e.g., longer settling time). For these reasons, this brief proposes a novel control scheme that explicitly accounts for the saturation in the controller and leads to superiorly fast and precise step tracking performance.

In this brief, we first develop an inner-loop compensator in Section III, which combines a feedforward inversion and a high-gain feedback control structure to cope with the hysteresis and resonance vibrations. Second, we present the main contribution

Fig. 2. Block diagram of the PZT actuated nanopositioner plant model, where u_p is the applied voltage input, d indicates the input disturbances including the hysteresis effects, q is the charge between the PZT electrodes, y is the actual displacement of the PZT positioner, and y_m is the capacitive position sensor output.

Fig. 3. Frequency responses of the PZT nanopositioner model $P(s)$.

TABLE I
MODAL PARAMETERS OF $M(s)$

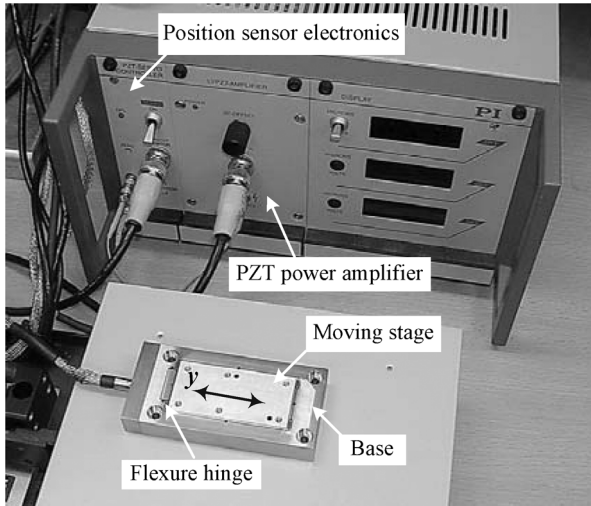| Mode (i)	ω_i	ζ_i	A_i	B_i
1	$2\pi 1018$	0.883	9.138×10^6	-736.62
2	$2\pi 2721$	0.051	-4.623×10^6	459.0
$D = 5.140 \times 10^{-3}$				

Fig. 1. Experimental setup of the PZT nanopositioner. (The PZT actuator and position sensor attached to the moving stage are embedded into the base.)

of this brief in Section IV where we explicitly model the PZT actuator as a saturated actuator, and the step tracking control problem is then casted as a linear quadratic control problem with input saturation. The solution of the problem eventually leads to a nested switching controller (NSC). Unlike the anti-windup compensator [18] and the non-saturated control design [19], the proposed NSC not only guarantees the stability in the presence of saturation, but also optimizes a quadratic performance function through properly oversaturating the controller that leads to desired fast convergence of the tracking error. Finally, experimental results are presented in Section V to demonstrate the effectiveness of the proposed design.

II. PLANT MODELING

Fig. 1 shows the experimental setup of the PZT nanopositioner (P-752, Polytec PI), which comprises a flexure-guided moving stage driven by a PZT microactuator with a travel range of ± 12.5 μm, and a capacitive position sensor with a practical resolution of 14 nm to measure the displacement of the moving stage along the axis. To clarify the associated dynamics and gains of the system, a block diagram is presented in Fig. 2. The voltage amplifier has an input limit $|u_p| \leq 4.4$ V corresponding to the PZT travel range. The nonlinear hysteresis effect of the PZT is modeled as a bounded input disturbance d. The PZT-flexure dynamics can be expressed as a sum of a number of resonance modes as follows:

$$M(s) = \sum_{i=1}^{N} \frac{B_i s + A_i}{s^2 + 2\zeta_i \omega_i s + \omega_i^2} + D \qquad (1)$$

where D is a feed-through term related to the zero locations of the system and it is found useful to better match the high-frequency roll-off characteristics; N is the total number of resonance modes of interest; ζ_i, ω_i, and A_i are the damping ratio, the resonance frequency and the modal constant, respectively; B_i is the resonance coupling parameter, which is used to match the non-minimum phase (NMP) characteristics.

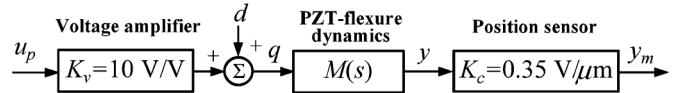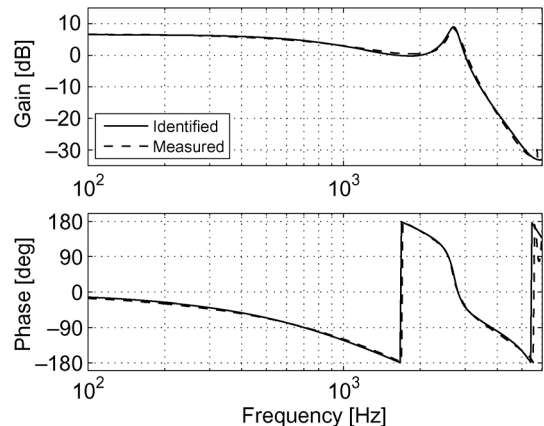The plant modal parameters can be identified from experimental frequency response data. Hence, we use a dynamic signal analyzer (HP 35670A) to collect the frequency response data for the plant model $P(s)$ expressed by

$$P(s) = \frac{y}{u_p} = K_v M(s). \qquad (2)$$

The dashed lines in Fig. 3 show the measured frequency responses of $P(s)$. We can see that the plant dynamics are dominated by two resonance modes whose resonance frequencies are 1018 and 2721 Hz, respectively. The first mode denotes the PZT electromechanical effect, whose resonance frequency typically decreases with a larger PZT capacitive load. Interested readers can refer to [11] for a detailed parameter electromechanical model. The second mode, caused by the flexibility of the flexure hinge, has a relatively large resonance peak around 10 dB and is thus expected to induce significant vibrations. From the phase plot in Fig. 3, we also observe that the phase exhibits extra lag (e.g., within 3–5 kHz) in addition to the phase lag associated with the resonance modes. This implies that the plant involves NMP anti-resonance modes (i.e., NMP zeroes).

By using the complex curve-fitting algorithm [20], the modal parameters of $M(s)$ can be identified as listed in Table I. Fig. 3 indicates that the identified model has a close match with the measured model. Moreover, we find that the resultant plant model $P(s)$ contains two pairs of complex NMP zeros [i.e., $10^4 \times (1.4834 \pm 1.3092j)$; $10^4 \times (0.5690 \pm 3.5087j)$], whose
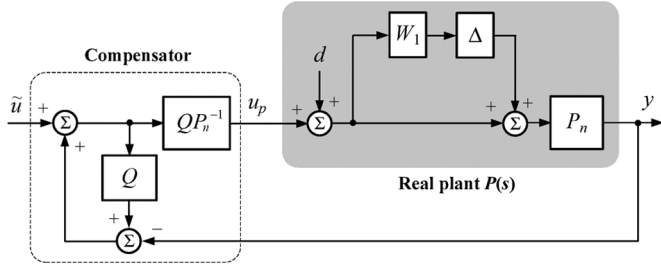
Fig. 4   Block diagram of inner-loop control system for hysteresis and resonance compensation.

Fig. 5.   Frequency response of nominal plant model P_n, perturbed plant models, and the relative uncertainty W_1 used for design and analysis. (Solid thick line: P_n; dashed lines: perturbed plant models; dashed-dotted line: W_1.)

resonance frequencies are located at 3151 and 5660 Hz, respectively. Due to the location adjacent to the resonance modes, these zero dynamics may come from the coupling between the PZT electromechanical effects and the flexure hinges. Note that these NMP zeros will substantially degrade the achievable control bandwidth, as will be clarified from the control analysis Section III.

III. HYSTERESIS AND RESONANCE COMPENSATION

This brief aims to design a feedback controller for fast step tracking in the presence of the nonlinear hysteresis, resonance vibrations, and control input saturation. In this section, we first study an inner-loop compensator using a combined feedforward/feedback control structure for hysteresis and resonance compensation.

A. Compensator Design

Fig. 4 shows the block diagram of the inner-loop control structure, which unifies high-gain feedback idea (through Q) and the feedforward inversion principle (through P_n^{-1}) to yield a closed-loop dynamics as specified by Q. In Fig. 4, the Q filter is the unique design parameter and we rewrite $P(s)$ as

$$P = P_n(1 + W_1\Delta). \qquad (3)$$

In the above, the nominal plant P_n represents the stable and minimum phase part of P, which can be obtained simply by removing the NMP zeros of P such that the resultant P_n satisfies

$$P_n \approx P \qquad (4)$$

within 0–200 Hz. $\|\Delta\|_\infty < 1$ denotes a stable unstructured disk-like uncertainty. W_1 represents a proper stable weighting function, which describes the NMP behavior of the plant and the plant uncertainties due to changes in the operating conditions such as PZT offset, reference input, and load variations. The magnitude of W_1 can be experimentally measured. More specifically, we collect 10 frequency responses data of $P_i(j\omega_k)$, $i = 1 \ldots 10$; $k = 1 \ldots 800$. Each measurement is carried out under a different operation condition. The dashed lines in Fig. 5 show the frequency responses of the perturbed plant models. Then, the magnitude of W_1 can be derived by

$$|W_1(j\omega_k)| = \max_{i=1\ldots10} \left(\frac{|P_i(j\omega_k) - P_n(j\omega_k)|}{|P_n(j\omega_k)|} \right) \qquad (5)$$
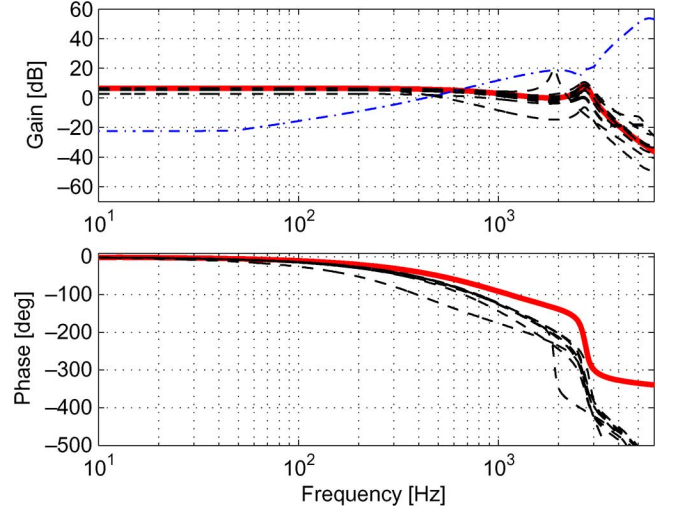
which is also plotted in Fig. 5. We can see that W_1 increases with frequency due to the relatively large uncertainty in high frequencies.

Next, we summarize and analyze the design conditions of Q filter to meet our desired performance.

i) $\|W_1Q\|_\infty < 1$. This condition is to guarantee the robust stability of the closed-loop system in Fig. 4, which has been proved in [21] using the small gain theorem.

ii) Q filter has low-pass characteristics such that

$$Q(j\omega) \approx 1, \quad \forall \omega \in [0, \ \omega_b] \qquad (6)$$

where ω_b denotes the frequency bandwidth of Q. To see the benefit of the Q with (6) and using (4), we derive the following transfer functions from respectively, the reference $\tilde{u}$ and the disturbance d to position output y:

$$T_{y\tilde{u}} = \frac{QPP_n^{-1}}{1 - Q\left(1 - PP_n^{-1}\right)} \approx Q \qquad (7)$$

$$T_{yd} = \frac{(1 - Q)P}{1 - Q\left(1 - PP_n^{-1}\right)} \approx 0 \qquad (8)$$

for $\omega \in [0, \ \omega_b]$. Note that these approximations are dependent on the approximation of (4) that is only valid within 0–200 Hz. Now it is clear that the closed inner-loop dynamics can be easily specified by Q and is capable of rejecting those disturbances at low frequency range such as hysteresis.

iii) $Q(j\omega_i) < -30$ dB, where ω_i ($i = 1, 2$) equals the PZT resonance frequencies as listed in Table I. This condition specifies the ratio of resonance compensation. Typically, a larger ratio of resonance compensation is at the expense of reduced frequency bandwidth of $Q(s)$. Due to this, the frequency bandwidth of $Q(s)$ is selected to be substantially lower than the first resonance frequency.

iv) $\Upsilon(Q) \geq \Upsilon(P_n)$, where Υ denotes the relative degree (excess of poles over zeros). This condition is imposed
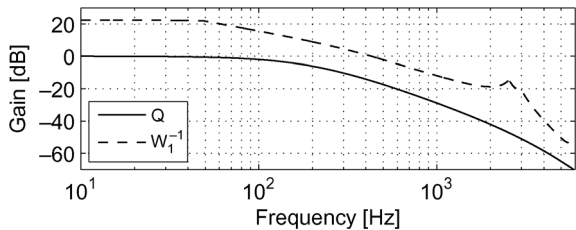
Fig. 6. Magnitude plots of W_1^{-1}, Q filter, and the measured closed inner-loop system $T_{y\tilde{u}}$. The robust stability condition $\|W_1 Q\|_\infty < 1$ is equivalent to $Q(j\omega)$ curve being below $W_1(j\omega)^{-1}$ curve. The magnitude of $T_{y\tilde{u}}$ indicates that the resonant peak of P at 2.7 kHz is greatly damped, which is consistent with the design.
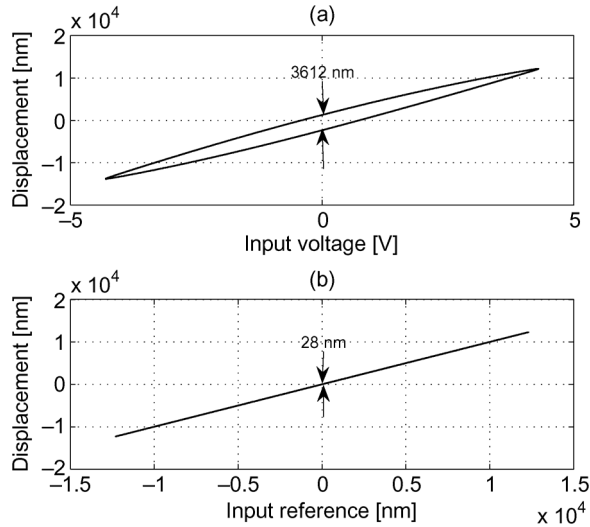

Fig. 7. Experimental results of hysteresis compensation. (a) Without compensator; (b) with compensator. The maximum gap between the hysteresis loop is significantly reduced from 3612 to 28 nm when the inner-loop compensator is applied.

to ensure that the controller QP_n^{-1} is proper, at least for practical implementation.

From the analysis above, the compensator design is simply reduced to the design of the Q filter only, which in our particular application is chosen as

$$Q = \frac{1}{(\tau_0 s + 1)^2 (\tau_1 s + 1)^3} \tag{9}$$

where $\tau_0 = 8.0 \times 10^{-4}$ and $\tau_1 = 3.2 \times 10^{-5}$. To verify the validity of the designed Q filter, Fig. 6 plots the magnitude of Q and W_1^{-1}, which indicates that the magnitudes of Q all lie below that of W_1^{-1} implying $\|W_1 Q\|_\infty < 1$. It is also straightforward to verify the satisfaction of the other design conditions in ii)–iv).

B. Performance of Hysteresis and Resonance Compensation

The designed compensator is implemented on a real-time DSP system (dSPACE-DS1103) with the sampling frequency of 20 kHz. First, we set the reference input $\tilde{u}$ to be a sinusoidal signal with the frequency of 0.1 Hz and with the amplitude that can drive the PZT actuator to work around its maximum range. Fig. 7 shows that without the inner-loop compensator the maximum gap between the hysteresis loop is 3612 nm, which is reduced to 28 nm with the compensator.
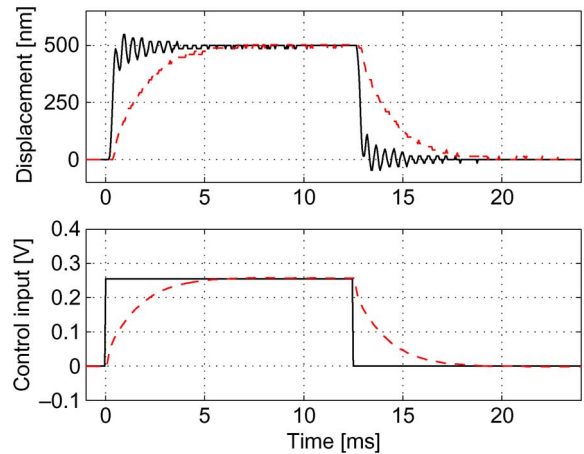

Fig. 8. Experimental results of repeated step tracking responses. The oscillations are almost removed with inner-loop compensator. The repeatability in the step responses indicates the robust performance of the compensator against the hysteresis with respect to various initial conditions. (Solid lines: Without compensator; dashed lines: with compensator.)

Next, the measured closed-loop system $T_{y\tilde{u}}$ as previously shown in Fig. 6 indicates that the resonant modes at 1018 and 2721 Hz are highly damped by more than 30 dB. Furthermore, the repeated step tracking results in Fig. 8 clearly show that the resonant vibrations are greatly suppressed with the compensator compared with those without the compensator. However, its transient response is relatively slow because the closed inner-loop bandwidth has to be reduced to provide sufficient stability margin. We also observe that the control input magnitude (the bottom plot of Fig. 8) is not necessarily much smaller than the PZT actuator input voltage limit (i.e., ± 4.4 V). To expedite the transient speed, we will propose an outer-loop control design in the next section that uses the maximum allowable PZT control input at the initial stage and then gradually decrease the control input when the PZT approaches the target. Additionally, Fig. 8 shows the repeatability in the step responses which indicates the robust performance of the compensator against the hysteresis with respect to various initial conditions.

Remark 1: This section is aimed to provide a simple design method for hysteresis and resonance compensation. The designed compensator is parameterized by a unique Q-filter based on which the robust stability condition is easily checked on the Bode plot (see Fig. 6) and the closed-loop dynamics is easily specified [see (7)]. We note that in terms of performance of hysteresis and resonance compensation, the proposed compensator is on par with existing control methods such as the PID control, the feedback-linearized inverse feedforward control [12] and the robust control [22].

IV. SATURATION CONTROL DESIGN

This section considers the designed inner-loop system. We firstly formulate the PZT step tracking control problem as a standard regulation control problem; and then we introduce the theory of linear quadratic (LQ) control with input saturation, based upon which a NSC is developed to improve the step tracking speed. The idea of NSC was originally proposed in [23]. Here, we will study its technical issues for the practical application to the PZT actuator.

A. Problem Formulation

Consider the system from $\tilde{u}$ to y in Fig. 4 with its state-space representation given by

$$\begin{cases} \dot{x}_p = Ax_p + \tilde{B}\sigma_p(\tilde{u}), & x_p(0) = x_p0 \\ y = Cx_p \end{cases} \qquad (10)$$

where x_p is the state of the inner-loop system, and the saturation function $\sigma_p(\tilde{u})$ defined as

$$\sigma_p(\tilde{u}) = \text{sgn}(\tilde{u})\min\{\bar{u}, |\tilde{u}|\} \qquad (11)$$

where $\bar{u} = 12.5$ is the saturation level of the control input which, in our case, equals to the PZT maximum travel range.

The objective here is to design an optimal $\tilde{u}$ subject to the actuator saturation to cause the output y to track a step input y_r rapidly without experiencing large overshoot. Let

$$\tilde{u} = \sigma_s(u_s) + Hy_r \qquad (12)$$

where y_r is the step input, u_s the control input to be designed as will be discussed later, $H = -(CA^{-1}\tilde{B})^{-1}$, and $\sigma_s(\cdot)$ is defined as in (11) with the saturation level

$$\bar{u}_s = \bar{u} - |Hy_r| \qquad (13)$$

where $|Hy_r| \leq \bar{u}$. Note that here A is an asymptotically stable matrix and thus H is well defined. Furthermore, define $x_r := -A^{-1}\tilde{B}Hy_r$ and let $x_e = x_p - x_r$, it is simple to transform (10) into

$$\dot{x}_e = Ax_e + \tilde{B}\sigma_p(\tilde{u}) = Ax_e + \tilde{B}\sigma_s(u_s) + Ax_r + \tilde{B}Hy_r + A^{-1}\tilde{B}H\dot{y}_r.$$

Noting that

$$Ax_r + \tilde{B}Hy_r + A^{-1}\tilde{B}H\dot{y}_r = 0. \qquad (14)$$

Therefore, the closed-loop system is given by

$$\dot{x}_e = Ax_e + \tilde{B}\sigma_s(u_s), \quad x_e(0) = x_e0. \qquad (15)$$

To this end, we formulate the outer-loop control design as a regulation control problem with input saturation. Next, we aim to find a state feedback control law u_s such that x_e converges to the origin rapidly. Once this is achieved, it indicates that $\lim_{t\to\infty} x_p(t) = x_r$. Therefore, $\lim_{t\to\infty} y(t) = Cx_r = -CA^{-1}\tilde{B}Hy_r = y_r$.

B. LQ Control With Input Saturation

Consider the system in (15). For the sake of easy presentation, we replace the pair $(x_e, u_s, \tilde{B})$ with (x, u, B) and hence (15) can be rewritten as

$$\dot{x} = Ax + B\sigma(u), \quad x(0) = x_0 \qquad (16)$$

where $x = x_e$, $B = \tilde{B}\bar{u}_s$, $u_s = u\bar{u}_s$ with $\bar{u}_s$ as (13), and $\sigma(\cdot)$ with saturation level equal to 1.
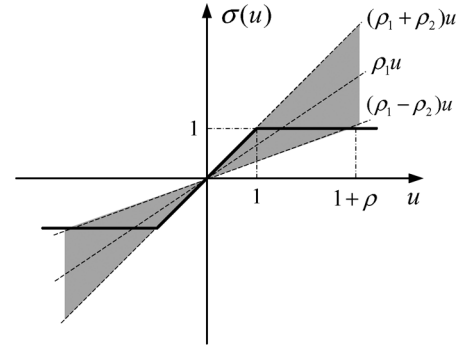

Fig. 9. Illustration of sector bound for $\sigma(u)$, where ρ is the level of over-saturation; the shaded area indicates the smallest sector to bound the saturation nonlinearity provided $|u| \leq 1 + \rho$; and ρ_1, ρ_2 are the values to model this sector.

Next, we consider the following quadratic cost function:

$$J(x_0, u) = \int_0^\infty \left(x^T\bar{Q}x + r\sigma(u)^2\right) dt \qquad (17)$$

for some $\bar{Q} = \bar{Q}^T > 0$ and $r > 0$ with (A, B) being controllable. Ideally, we aim to seek an optimal linear state feedback $u = Kx$ for each given initial state x_0 such that $J(x_0, u)$ is minimized. It is well-known that if the control is not saturated, the optimal solution to K is given by

$$K = -r^{-1}B^T\bar{P}_0 \qquad (18)$$

where $\bar{P}_0 = \bar{P}_0^T > 0$ is the solution to the following Ricatti equation:

$$A^T\bar{P}_0 + \bar{P}_0A + \bar{Q} - r^{-1}\bar{P}_0BB^T\bar{P}_0 = 0. \qquad (19)$$

Moreover, the minimal cost is given by $x_0^T\bar{P}_0x_0$.

However, in the presence of saturation, the optimal K is difficult to give. To overcome this difficulty, we parameterize the controller by using an optimal sector bound [23]. More specifically, define the level of over-saturation $\rho \geq 0$ such that the control input u is restricted to be

$$|u| \leq 1 + \rho. \qquad (20)$$

It is easy to verify that for any u constrained by (20), $\sigma(u)$ lies in the following sector bound as illustrated in Fig. 9:

$$\sigma(u) = \rho_1 u + \delta(u) \qquad (21)$$

$$|\delta(u)| \leq \rho_2 u, \quad \forall |u| \leq 1 + \rho \qquad (22)$$

where

$$\rho_1 = \frac{2+\rho}{2(1+\rho)}, \quad \rho_2 = \frac{\rho}{2(1+\rho)}. \qquad (23)$$

Now, for a given $\rho > 0$, we consider the Lyapunov function candidate $V(x) = x^T\bar{P}_\rho x$ for some $\bar{P}_\rho = \bar{P}_\rho^T > 0$ to be designed and define

$$\Omega_\rho = A^T\bar{P}_\rho + \bar{P}_\rho A + \bar{Q} - r^{-1}\bar{P}_\rho BB^T\bar{P}_\rho. \qquad (24)$$

Given any initial state x_0 and any $\delta(\cdot)$ satisfying (22), it is easy to verify that

$$
\begin{aligned}
J(x_0, u, T) &= V(x_0) - V(x(T)) \\
&+ \int_0^T \left(\frac{d}{dt} V(x) + x^T \bar{Q} x + r\sigma(u)^2 \right) dt \\
&\leq V(x_0) + \int_0^T f(x, u, \delta(u)) \, dt
\end{aligned}
$$

where

$$
f(x, u, \delta(u)) = x^T \Omega_\rho x + r \left(\rho_1 u + \delta(u) + r^{-1} B^T \bar{P}_\rho x \right)^2. \tag{25}
$$

This implies that if $f(x, u, \delta(u)) \leq 0$ for all $x \in \mathbb{R}^n$ and $\delta(\cdot)$ satisfying (22), then

$$
J(x_0, u) \leq V(x_0). \tag{26}
$$

From the analysis above, we formulate the following relaxed optimal control problem.

P1: For a given $\rho \geq 0$, design $\bar{P}_\rho$ and u to minimize $V(x_0)$ subject to $f(x, u, \delta(u)) \leq 0$ for all $x \in \mathbb{R}^n$ and $\delta(\cdot)$ satisfying (22). Moreover, determine the largest invariant set X_ρ characterized by an ellipsoid of the form

$$
X_\rho = \left\{ x : x^T \bar{P}_\rho x \leq \mu_\rho^2 \right\}, \quad \mu_\rho > 0 \tag{27}
$$

such that if $x_0 \in X_\rho$, $x(t) \in X_\rho$ and $|u(t)| \leq 1 + \rho$ for all $t \geq 0$, we have $J(x_0, u) \leq V(x_0)$.

The solution to the above problem is given as follows:

Theorem 1: [23]: Consider the system in (23) and the cost function in (16). For a given level of over-saturation $\rho \geq 0$, suppose the equation

$$
A^T \bar{P}_\rho + \bar{P}_\rho A + \bar{Q} - r^{-1} \left(1 - \rho_0^2 \right) \bar{P}_\rho B B^T \bar{P}_\rho = 0 \tag{28}
$$

where

$$
\rho_0 = \frac{\rho_2}{\rho_1} = \frac{\rho}{2 + \rho} \tag{29}
$$

has a solution $\bar{P}_\rho = \bar{P}_\rho^T > 0$. Then the optimal feedback control law K_ρ for the relaxed optimal control problem *P1* is given by

$$
K_\rho = -\rho_1^{-1} r^{-1} B^T \bar{P}_\rho \tag{30}
$$

and the associated invariant set X_ρ is bounded by

$$
\mu_\rho = \frac{r}{(1 - \rho_0) \sqrt{B^T \bar{P}_\rho B}}. \tag{31}
$$

Remark 2: If $\rho = 0$, the Riccati equation (28) and the control law (30) recover the results in (19) and (18) for optimal control without saturation. The associated invariant set is given by

$$
X_0 = \left\{ x : x^T \bar{P}_0 x \leq \mu_0^2 \right\}, \quad \mu_0 = \frac{r}{\sqrt{B^T \bar{P}_0 B}}. \tag{32}
$$

Remark 3: Despite that the invariant set enlarges when ρ increases, it can be seen that the upper bound of the performance

cost in (26) becomes larger. This implies that the saturated controller can bring a good benefit when ρ is not close to 0 and not too large. Generally, ρ can be selected as the minimal one satisfying $x_0 \in X_\rho$.

1) Properties of the Control Law: The proposed controller in Theorem 1 has two nice properties, i.e., the nesting property of X_ρ and monotonicity of $\bar{P}_\rho$. More specifically, define

$$
S_\rho = (1 - \rho_0) \bar{P}_\rho. \tag{33}
$$

We can rewrite the Riccati equation in (28) as

$$
A^T S_\rho + S_\rho A + (1 - \rho_0) \bar{Q} - r^{-1}(1 + \rho_0) S_\rho B B^T S_\rho = 0 \tag{34}
$$

and the invariant set can be expressed as

$$
X_\rho = \left\{ x : x^T S_\rho x \leq \frac{r^2}{B^T S_\rho B} \right\}. \tag{35}
$$

Lemma 1: [23]: The solution S_ρ to (34) is monotonically decreasing in $\rho > 0$, i.e., for a sufficiently small $\epsilon > 0$, $S_\rho > S_{\rho+\epsilon}$, if $0 \leq \rho < \rho + \epsilon$. Consequently, X_ρ are nested in the following sense:

$$
X_\rho \subset X_{\rho+\epsilon}, \quad \forall 0 \leq \rho < \rho + \epsilon. \tag{36}
$$

Moreover, the solution $\bar{P}_\rho$ to the Riccata equation in (28) is monotonically increasing in $\rho > 0$. That is

$$
P_\rho < P_{\rho+\epsilon}, \quad \forall 0 \leq \rho < \rho + \epsilon. \tag{37}
$$

C. Nested Switching Control

Thanks to the nesting property of X_ρ and monotonicity of $\bar{P}_\rho$, we can apply Theorem 1 to design a sequence of control gains K_i, based on which a nested switching control can be developed to improve the performance. More specifically, we choose a sequence of over-saturation bounds $0 = \rho_0 < \rho_1 < \cdots < \rho_N$ and then solve the corresponding Lyapunov matrices $\bar{P}_i$, invariant sets X_i and controller gains K_i, $i = 0, 1, \ldots, N$. Finally, we can construct the nested switching control law by selecting the control gain K_i when $x \in X_i$ and $x \notin X_{i-1}$ (unless $i = 0$). The following result shows the advantage of the nested switching control in the performance improvement.

Lemma 2 [23]: Suppose the switching controller above is applied to the system in (16) with $x_0 \in X_N$, Let t_i be the time instance K_i is switched on, $i = 0, 1, \ldots, N$, particularly, $t_N = 0$. Then the cost of the switching control is bounded by

$$
\begin{aligned}
J(x_0, u) &\leq x_0^T \bar{P}_N x_0 - \sum_{i=0}^{N-1} x^T(t_i)(\bar{P}_{i+1} - \bar{P}_i)x(t_i) \\
&< x_0^T \bar{P}_N x_0. \tag{38}
\end{aligned}
$$

From the lemma above, we can clearly see the advantage of the switching control by means of the negative term in (38) that decreases the cost gradually. In what follows, we will discuss how to choose $\bar{Q}$, r, and ρ_i and then apply the nested switching control to the PZT actuator for improved tracking performance.

D. Guidelines of Selecting $\bar{Q}$, r, and ρ_i

Since the main purpose of using nested switching control is to speed up the transient response, it is intuitive to inject the maximum control input (by applying a large control gain K_i, $i > 0$) to achieve the fastest acceleration at the initial stage when the controlled output y is far away from the set point. When the controlled output y approaches the final set point, the control input should be gradually decreased (by applying a small control gain K_0) for a smaller overshoot. Such a control strategy would impose some conditions on $\bar{Q}$, r, and ρ_i.

First, we consider the case where controlled output y is close to the set point so as that the control gain K_0 (i.e., $\rho_0 = 0$) is applied. Under such a circumstance, the control input is not saturated. It is straightforward to verify that the closed-loop system can be expressed as

$$\dot{x} = (A - BB^T \bar{P}_0)x. \tag{39}$$

Clearly, we can select $\bar{Q}$ and r (hence corresponding to a unique solution of $\bar{P}_0$) such that the dominated poles of $A - BB^T\bar{P}_0$ should have a large damping ratio, which in turn will generate a small overshoot.

Second, to achieve a fast tracking speed when the controlled output y is far away from the set point, a larger control gain K_i corresponding to a $\rho_i > 0$ should take action prior to K_0. This implies that the associated invariant set X_0 as given by (32) should be as small as not to cover the initial state $x(0)$. Therefore, an additional stringent constraint is imposed on $\bar{Q}$ for such an X_0.

Finally, for the given $\bar{Q}$ and r determined from the above, according to Remark 4, choose ρ_N as the minimum satisfying $x(0) \in X_N(\rho_N)$. Subsequently, choose ρ_i with $0 < \rho_i < \rho_N$ provided that inserting the resulting K_i can bring further performance improvement (e.g., reducing steady-state chattering). Note that the control gain K_N associated with ρ_N will generally cause the control input to hit its saturation level at the initial stage for the purpose of maximum acceleration.

More specifically, the following procedure summarizes the guidelines for selecting $\bar{Q}$, r, and ρ_i.
1) Without loss of generality, we set $r = 1$ since the performance cost can be normalized as J/r.
2) Given y_r and the resultant pair (A, B), select a $\bar{Q} = \bar{Q}^T > 0$ and solve (19) for a $\bar{P}_0$ such that the resulting closed-loop system matrix $A - BB^T \bar{P}_0$ has the desired poles locations, particularly, the dominated poles should have a large damping ratio. The solution of $\bar{P}_0$ can be easily obtained using the MATLAB command (care).
3) Calculate μ_0 using (32) and the initial state with

$$x(0) = x_{p0} - A^{-1}\tilde{B}(CA^{-1}\tilde{B})^{-1} y_r. \tag{40}$$

Check if $x(0)^T \bar{P}_0 x(0) > \mu_0^2$. If not, we go back to previous step and re-select $\bar{Q}$. Generally, increasing $\bar{Q}$ is effective due to the monotonicity property of the solution of the Riccati equation (19).
4) Solve $x(0)^T \bar{P}_N x(0) = \mu_N^2$ to yield ρ_N.
5) Evaluate the closed-loop performance by applying K_0 and K_N only (i.e., with the minimum switching controllers). If the control output y exhibits unacceptable overshoot or

chattering in steady state, insert an interim controller K_i with $0 < \rho_i < \rho_N$ and so forth until the performance is acceptable.

E. Application to PZT Tracking Control

The complete PZT model considered for tracking control is shown in (7). However, in this design stage, we consider an approximate second-order model given by

$$\dot{x}_p = \begin{bmatrix} 0 & 1 \\ a_1 & a_2 \end{bmatrix} x_p - \begin{bmatrix} 0 \\ \tilde{b} \end{bmatrix} \sigma_p(\tilde{u}), \quad x_p(0) = 0$$
$$y = \begin{bmatrix} 1 & 0 \end{bmatrix} x_p \tag{41}$$

where $x_p = [y \; \dot{y}]^T$, $a_1 = -1.1109 \times 10^6$, $a_2 = -1.9227 \times 10^3$, $\tilde{b} = 1.1409 \times 10^6$.

Since we aim for fast settling-time performance, we also define the *settling time* as the total time that it takes for the position output to enter and remain within ± 30 nm of the target set point. Note that as the position sensor has a resolution of ± 14 nm, the specified position precision of 30 nm is almost the best achievable in practice.

We now follow the above procedure to design an NSC for this system and take the reference with $y_r = 500$ nm as a design example. After few iterations, we obtain $\bar{Q} = [9.9364 \; 0; 0 \; 2.9 \times 10^{-8}]^T$, which leads to the closed-loop damping ratio 0.785 and $\rho_1 = 13$. We begin with using two switching controllers. This leads to the controller gains

$$K_0 = -[2.141 \; 0.0009], \quad K_1 = -[5.6915 \; 0.0027] \tag{42}$$

and the corresponding Lyapunov matrices $\bar{P}_i$ and regions of attraction μ_i are given by, respectively

$$\bar{P}_0 = \begin{bmatrix} 7.6286 \times 10^{-3} & 2.3457 \times 10^{-6} \\ 2.3457 \times 10^{-6} & 1.0076 \times 10^{-9} \end{bmatrix}, \quad \mu_0 = 0.0345$$

$$\bar{P}_1 = \begin{bmatrix} 9.3673 \times 10^{-3} & 3.3405 \times 10^{-6} \\ 3.3405 \times 10^{-6} & 1.6059 \times 10^{-9} \end{bmatrix}, \quad \mu_1 = 0.205.$$

Consequently, the switching logic can be described as follows.
- Controller gain K_1 in (42) is switched on when $[y \; \dot{y}]\bar{P}_1[y \; \dot{y}]^T \leq \mu_1^2$ and $[y \; \dot{y}]\bar{P}_0[y \; \dot{y}]^T > \mu_0^2$.
- Controller gain K_0 in (42) is switched on when $[y \; \dot{y}]\bar{P}_0[y \; \dot{y}]^T \leq \mu_0^2$.

Note that the control algorithm ensures that there is only one controller active at any time instance.

For comparison, we also design the following implementable PID controller:

$$u = \left(0.42 + \frac{17.5}{s} + \frac{7 \times 10^{-5} s}{6.36 \times 10^{-5} s + 1} \right) (y_r - y) \tag{43}$$

which can achieve the minimum settling time with non-saturated control input.

V. EXPERIMENTAL RESULTS

The designed tracking controllers are implemented on the PZT nanopositioner, where we use backward differentiation of the position signals cascaded with an appropriate noise filter to estimate the velocity. Firstly, we compare the performance between the NSC and its non-switching case (i.e., with only a single set of gain K_1) with the step responses to $y_r = 500$ nm
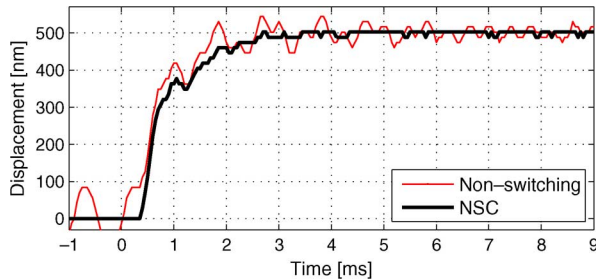
Fig. 10. Comparison of step responses between NSC and its non-switching case. The NSC is more effective to reduce the vibrations in steady state since a smaller gain is switched on when the output approaches the target.
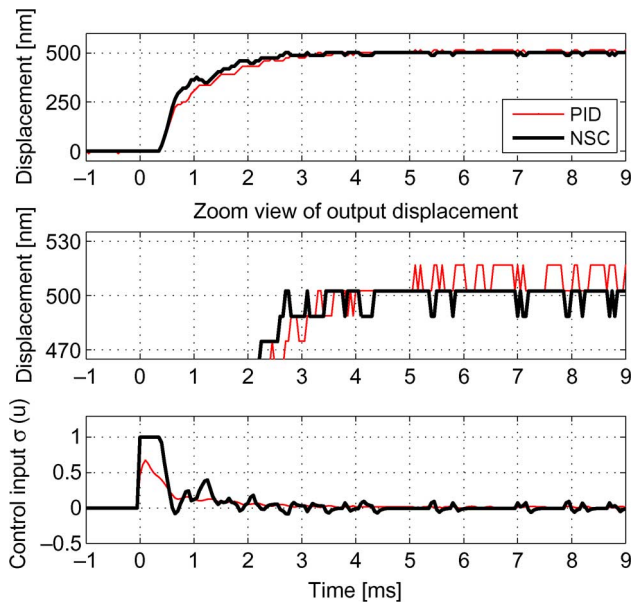

Fig. 11. Comparison of step responses between NSC and PID. The NSC achieves faster settling time by properly saturating the control input.

TABLE II
COMPARISON OF THE SETTLING TIME IMPROVEMENT

Step Length	Settling Time (ms)		Improvement
(nm)	PID	NSC	(%)
50	0.572	0.505	12
500	2.683	2.233	17
3000	3.7	3.1	16
10000	5.065	3.49	31

shown in Fig. 10. We can see that the NSC exhibits much less vibrations in steady state because a smaller gain is switched on when the output approaches the target. Second, we compare the performance between the NSC and the PID. The experimental results are shown in Fig. 11. We can see that compared with PID, the NSC significantly reduces the settling time. We have also implemented other step responses over the full PZT operational range and the results are summarized in Table II. We can see that the settling time under the NSC is greatly reduced by more than 12% compared with the PID.

VI. CONCLUSION

We have proposed a new fast tracking control method, the so-called NSC, for the PZT actuator. The NSC is developed with the actuator saturation considered explicitly in the design process. Distinct from conventional control, the proposed NSC can guarantee the closed-loop system stability in the presence of saturation, meanwhile significantly improve the tracking speed through switching the controllers that optimize a quadratic cost function. The experimental results demonstrate that the NSC has outperformed the PID control by more than 12% in settling time within almost the full PZT operational range.

REFERENCES

[1] C. Mio, T. Gong, A. Terray, and D. Marr, "Design of a scanning laser optical trap for multiparticle manipulation," *Rev. Sci. Instrum.*, vol. 71, no. 5, pp. 2196–2200, May 2000.
[2] H. Liaw, B. Shirinzadeh, and J. Smith, "Robust motion tracking control of piezo-driven flexure-based four-bar mechanism for micro/nano manipulation," *Mechatronics*, vol. 18, pp. 111–120, 2008.
[3] G. Binnig, C. Quate, and C. Gerber, "Atomic force microscope," *Phys. Rev. Lett.*, vol. 56, no. 9, pp. 930–933, Mar. 1986.
[4] A. Fleming and R. Moheimani, "Precision current and charge amplifiers for driving highly capacitive piezoelectric loads," *Electron. Lett.*, vol. 39, no. 3, pp. 282–284, Feb. 2003.
[5] R. Moheimani and B. Vautier, "Resonant control of structural vibration using charge-driven piezoelectric actuators," *IEEE Trans. Control Syst. Technol.*, vol. 13, no. 6, pp. 1021–1035, Nov. 2005.
[6] S. Devasia, E. Eleftheriou, and R. Moheimani, "A survey of control issues in nanopositioning," *IEEE Trans. Control Syst. Technol.*, vol. 15, no. 5, pp. 802–823, Sep. 2007.
[7] G. Clayton, S. Tien, K. Leang, Q. Zou, and S. Devasia, "A review of feedforward control approaches in nanopositioning for high-speed SPM," *J. Dyn. Syst., Meas. Control*, vol. 131, pp. 061101-1–061101-19, Nov. 2009.
[8] D. Croft, G. Shed, and S. Devasia, "Creep, hysteresis, and vibration compensation for piezoactuators: Atomic force microscopy application," *J. Dyn. Syst., Meas. Control*, vol. 123, pp. 35–43, Mar. 2001.
[9] J. Yi, S. Chang, and T. Shen, "Disturbance-observer-based hysteresis compensation for piezoelectric actuators," *IEEE/ASME Trans. Mechatron.*, vol. 14, no. 4, pp. 456–464, Aug. 2009.
[10] A. Visintin, , G. Bertotti and I Mayergoyz, Eds., "Mathematical models of hysteresis," in *The Science of Hysteresis*. London, U.K.: Academic, 2006, pp. 1–123.
[11] M. Goldfarb and N. Celanovic, "A lumped parameter electromechanical model for describing the nonlinear behavior of piezoelectric actuators," *J. Dyn. Syst., Meas., Control*, vol. 119, pp. 478–485, Sep. 1997.
[12] K. Leang and S. Devasia, "Feedback-linearized inverse feedforward for creep, hysteresis, and vibration compensation in AFM piezoactuators," *IEEE Trans. Control Syst. Technol.*, vol. 15, no. 5, pp. 927–935, Sep. 2007.
[13] B. Bhikkaji and R. Moheimani, "Integral resonant control of a piezoelectric tube actuator for fast nanoscale positioning," *IEEE/ASME Trans. Mechatron.*, vol. 13, no. 5, pp. 530–537, Oct. 2008.
[14] C. Li, H. Beigi, S. Li, and J. Liang, "Nonlinear piezo-actuator control by learning self tuning regulator," *J. Dyn. Syst., Meas. Control*, vol. 115, pp. 720–723, Dec. 1993.
[15] A. Sebastian and S. Salapaka, "Design methodologies for robust nanopositioning," *IEEE Trans. Control Syst. Technol.*, vol. 13, no. 6, pp. 868–876, Nov. 2005.
[16] S. Tien, Q. Zou, and S. Devasia, "Iterative control of dynamics-coupling-caused errors in piezoscanners during high-speed AFM operation," *IEEE Trans. Control Syst. Technol.*, vol. 13, no. 6, pp. 921–931, Nov. 2005.
[17] Q. Zou and S. Devasia, "Preview-based optimal inversion for output tracking: Application to scanning tunneling microscopy," *IEEE Trans. Control Syst. Technol.*, vol. 12, no. 3, pp. 375–386, May 2004.
[18] N. Kapoor, A. Teel, and P. Daoutidis, "An anti-windup design for linear systems with input saturation," *Automatica*, vol. 34, pp. 559–574, 1998.

[19] B. Chen, T. Lee, K. Peng, and V. Venkataramanan, "Composite non-linear feedback control for linear systems with input saturation: Theory and an application," *IEEE Trans. Autom. Control*, vol. 48, no. 3, pp. 427–439, Mar. 2003.

[20] E. Levi, "Complex-curve fitting," *IRE Trans. Autom. Control*, vol. AC-4, pp. 37–44, 1959.

[21] N. Bajcinca and T. Bunte, "A novel control structure for dynamic inversion and tracking tasks," in *Proc. 16th IFAC World Congr.*, 2005, pp. 277–282.

[22] S. Salapaka, A. Sebastian, J. Cleveland, and M. Salapaka, "High bandwidth nano-positioner: A robust control approach," *Rev. Scientific Instrum.*, vol. 73, no. 9, pp. 3232–3241, Sep. 2002.

[23] M. Fu, "Linear quadratic control with input saturation," presented at the Robust Control Workshop, Newcastle, U.K., 2000.